



Masters, D., Poole, D., Taylor, N., Rendall, T., & Allen, C. (2017). Influence of shape parameterisation on a benchmark aerodynamic optimisation problem. *Journal of Aircraft*.

Peer reviewed version

[Link to publication record in Explore Bristol Research](#)
PDF-document

This is the author accepted manuscript (AAM). The final published version (version of record) is available online via ARC at <https://arc.aiaa.org/doi/10.2514/1.C034006>. Please refer to any applicable terms of use of the publisher.

University of Bristol - Explore Bristol Research

General rights

This document is made available in accordance with publisher policies. Please cite only the published version using the reference above. Full terms of use are available:
<http://www.bristol.ac.uk/pure/about/ebr-terms.html>

Influence of Shape Parameterisation on a Benchmark Aerodynamic Optimisation Problem

D. A. Masters^{*}, D. J. Poole[†],

Department of Aerospace Engineering, University of Bristol

N. J. Taylor[‡],

MBDA UK Ltd, Filton

T. C. S. Rendall[§] and C. B. Allen[¶]

Department of Aerospace Engineering, University of Bristol

This paper presents an investigation into the influence of shape parameterisation and dimensionality on the optimisation of a benchmark case described by the AIAA Aerodynamic Design Optimisation Discussion Group. This problem concerns the drag minimisation of a NACA0012 under inviscid flow conditions at $M = 0.85$ and $\alpha = 0$ subject to a local thickness constraint. The work presented here applies six different shape parameterisation schemes to this optimisation problem with between 4 and 40 design variables. The parameterisation methods used are: Bèzier Surface FFD; B-Splines; CSTs; Hicks-Henne bump functions; a Radial Basis Function domain element method (RBF-DE) and a Singular Value Decomposition (SVD) method. The optimisation framework used consists of a gradient based SQP optimiser coupled with the SU² adjoint Euler solver which enables the efficient calculation of the design variable gradients. Results for all the parameterisation methods are presented with the best results for each technique converging to two distinct optimised aerofoil shapes with drag counts ranging between 25 and 56 (from an initial value of 469). The optimal result was achieved with the B-Spline method with 16 design variables. Further analysis of results is then presented to investigate the design spaces, numerical error, flow behaviour and the presence of hysteresis.

I. Introduction

Optimisation in engineering typically requires the integration of a number of complex numerical techniques into an automated, objective-driven design procedure. In practice this requires the selection of a range of methods or software packages to cover the specific set of tasks required. Within aerodynamic shape optimisation this typically means selecting from a wide range of shape parameterisation, mesh generation/deformation, flow/gradient calculation and optimisation algorithms to assemble a complete optimisation framework. To aid the assessment of these frameworks a series of benchmark cases have been set out by AIAA Aerodynamic Design Optimisation Discussion Group (ADODG)^a to allow comparisons to be made on identical test cases. However with so many factors affecting each optimisation it can still be very difficult to isolate the influence of each individual component. This paper aims to investigate the influence of shape parameterisation methods on aerodynamic optimisation by comparing a range of methods for ADODG benchmark case one. This is a two-dimensional, inviscid, symmetric drag minimisation case.

A wide range of methods have previously been used for aerofoil geometry representation. These vary from general curve representation techniques such as B-Splines to free-form deformation deformation methods such as Bèzier surfaces¹ or radial basis functions². One of the simplest forms of parameterisation is the discrete (or free-surface) method. This directly uses the surface points of a discretely defined aerofoil as the design variables³. The benefit of this is that it allows extremely fine control over the shape with absolutely no restriction on the design space. The size and complexity of the resulting optimisation problem can however cause significant difficulties, such as slow convergence or unsmooth aerofoils. For these reasons more robust and efficient parameterisation methods are usually favoured.

^{*}Graduate Student, AIAA Student Member, dominic.masters@bristol.ac.uk, Bristol, BS8 1TR, UK

[†]Graduate Student, AIAA Student Member, d.j.poole@bristol.ac.uk, Bristol, BS8 1TR, UK

[‡]Capability Leader, Aerodynamic Tools & Methods, AIAA Senior Member, nigel.j.taylor@mbda-systems.com, WG3, PO Box 5, Filton, Bristol, BS34 7QW, UK

[§]Lecturer, AIAA Member, thomas.rendall@bristol.ac.uk, Bristol, BS8 1TR, UK

[¶]Professor of Computational Aerodynamics, AIAA Senior Member, c.b.allen@bristol.ac.uk, Bristol, BS8 1TR, UK

^a<https://info.aiaa.org/tac/ASG/APATC/AeroDesignOpt-DG>

Hicks and Henne's⁴ early analytical approach based on bump functions represents one alternative. It takes a base aerofoil and then adds a linear combination of single-signed sine functions to deform its upper and lower surfaces to create a new aerofoil shape. This concept of adding a linear combination of simple basis functions to a base shape has also been used by Kulfan's CST^{5,6} method. This adds a combination of Bernstein polynomials to a simple, analytical 'aerofoil class' shape. Both of these methods have seen frequent use within the framework of aerodynamic optimisation⁷⁻¹⁷.

Other methods, such as B-Splines or polynomial fitting are also commonly used. B-Splines represent a class of versatile, piecewise polynomial, control point based curves with variable continuity and support. Due to their intuitiveness and flexibility they have been applied to a wide range of applications with extensive use throughout shape optimisation including a range of aerofoil specific cases¹⁸⁻²⁹. Sobieczky's³⁰ PARSEC (Parameterised Sections) method is also popular, approximating each surface by a 6th order polynomial. However, as the method is limited to only 12 design variables it does not provide the range or flexibility in fidelity made available by many of its alternatives.

Attempts have also been made to mathematically derive a set of orthogonal modes to represent an aerofoil. This is typically done through the proper orthogonal decomposition of a set of training aerofoils which will create a set of optimal orthogonal shape modes based on a range of training data. Studies of this nature have been produced by Toal *et al.*³¹, Ghoman *et al.*³² and then by Poole *et al.*³³ who used a large, varied collection of aerofoils and singular value decomposition (SVD) method to produce a universal set of modes representing the deformation of aerofoil shapes.

Another approach to shape parameterisation is to use free-form deformation (FFD) which is a method typically used in soft object animation. This creates a smooth continuous volume transformation based on the change in position of a series of control points. This volume transformation can also be used to deform computational volume meshes seamlessly with the aerofoil. This can have significant cost benefits particularly in three dimensions. The two principal FFD techniques in use are radial basis functions domain element methods (RBF-DEs)² applied on an arbitrary domain element (a series of user positioned initial control points), and Bèzier surfaces¹ (often referred to as just 'FFD') which use a structured lattice of initial control points. Both of these methods have shown promising optimisation results³⁴⁻⁴⁰.

ADODG test case one has previously been investigated with a variety of these techniques: B-Splines²¹⁻²⁹; Free-Surface^{22,28}; CSTs¹⁵⁻¹⁷; Hicks-Henne bump functions¹⁴; Bèzier Surface FFD³⁸; PARSEC⁴¹; RBF-DEs^{39,40} and SVDs^{40,42}. Even though this represents a significant test sample for comparison of the parameterisation methods, due to the large range of factors influencing each result, it is still difficult to isolate their contribution. For example, the choice of flow solver⁴³ or optimisation algorithm⁴⁰ has been shown to have a significant impact on the optimisation results for this case. For this reason this work applies a large range of parameterisation methods to this case under the same optimisation framework to provide an unbiased platform for comparison.

The optimisation framework is completed with three well established and robust techniques. The mesh generation is handled by a structured conformal mapping method coupled with an RBF mesh deformation technique⁴⁴ (this is entirely separate from the RBF parameterisation). The flow solution and gradients are calculated using SU2⁴⁵ and the optimisation is carried out using the gradient-based SQP optimiser SNOPT⁴⁶. All of these have been commonly used for aerodynamic optimisation^{13,16,21,23-25,34-36,40,42}.

In this work a range of shape parameterisation techniques have been applied to ADODG benchmark case one with between four and 40 design variables to assess and compare the performance of each method. Further analysis techniques have then been applied to final optimised shapes to further understand the design spaces, numerical error, flow behaviour and the presence of hysteresis.

II. NACA0012 Inviscid Drag Optimisation

A. Case Specifications

The benchmark case⁴⁷ considered in this paper is the inviscid, drag minimisation of a NACA0012 with freestream Mach number (M) of 0.85 subject to a thickness constraint at zero degrees incidence (α). Formally described as

$$\begin{aligned} &\text{Minimise } C_D \\ &\text{subject to: } M = 0.85, \\ &\quad \alpha = 0, \\ &\quad z \geq z^{baseline} \quad \text{on upper surface } \forall x \in [0, 1], \\ &\quad z \leq z^{baseline} \quad \text{on lower surface } \forall x \in [0, 1]. \end{aligned}$$

This problem is based on work by Vassberg *et al.*²⁸ though with a slight modification to the baseline NACA0012 geometry to ensure a sharp trailing edge. It is defined as:

$$z^{baseline} = \pm 0.6(0.2969\sqrt{x} - 0.1260x - 0.3516x^2 + 0.2843x^3 - 0.136x^4). \quad (1)$$

This aerofoil produces approximately 469 drag counts for the design conditions and figure 1 shows the Mach contours of the flowfield. It can be seen that a large shock is present at approximately 75% chord. As viscosity is omitted, this shock is the source of all of the physical drag associated with this problem. This optimisation is therefore an exercise in minimising the size and strength of this shock and, consequently, the wave drag. It should be noted that a small amount of ‘numerical drag’ will also be calculated as a result of numerical error and therefore a shock-free solution may not exhibit exactly zero drag.

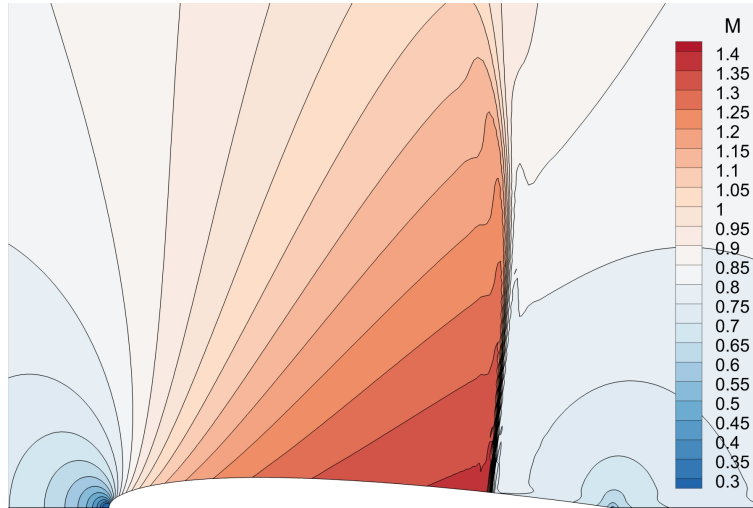


Figure 1. Flowfield plot for initial NACA0012 at $M = 0.85$.

B. Previous Work

This test case has been investigated a significant number of times previously with all cases reducing the drag by increasing the aerofoil thickness aft of the max thickness point. The best results typically exhibit drag ranging between 25 and 120 counts though many researchers reported problems obtaining monotonically decrease for increases in dimensionality^{22,24,25,40}. Additionally, many of these studies also reported a difficulty in sufficiently converging the KKT optimality condition for large design variables cases^{21,22,24,25,38}. It is possible that these difficulties are caused by the appearance of unexpected flow characteristics present for the highly optimised aerofoils. For example Meheut *et al.*⁴⁸ compared a number of optimised aerofoil shapes^{22,23,25,39,40,43} and noted the appearance of hysteresis at the design Mach number. They showed that for the aerofoil produced by Carrier *et al.*²² two possible solutions existed, one with ~60 drag counts and one with ~110 drag counts. Similar behaviour was found by Lee *et al.*²⁵ who found solutions with ~40 and ~130 drag counts; an even larger difference in drag. They also found solutions with non-zero lift and an asymmetric flow field despite the fully symmetrical problem and mesh. The occurrences of these unexpected lifting solutions (which produce high drag values) in the line searches was cited as a contributor to some of the optimisation procedures stagnating prematurely²⁵. Nadarajah²³ found similar problems, with the flow converging to oscillatory results due to the existence of multiple solutions. This was however overcome by enforcing a symmetry boundary condition along the wake. This single change improved the final result of an optimisation procedure significantly, reducing the drag from 55.3 to 37.5 counts on a 768×128 mesh. This result was then further reduced to 25.2 counts when run on a super-fine 3072×512 mesh.

III. Parameterisation Methods

This work considers the impact of shape parameterisation on the case outlined above. The six methods considered are: Bèzier Surface FFD; B-Splines; CSTs; Hicks-Henne bump functions; a Radial Basis Function domain element method (RBF-DE) and a Singular Value Decomposition (SVD) method. This section outlines these methods and their definitions.

A. Bèzier Surface FFD

A Bèzier surface is a B-spline surface of Bèzier curves. Although these are usually used to create surfaces in three-dimensional space, they can also be used as a deformation tool in two-dimensions by constraining the control points to a plane. To create a deformable domain from this surface a rectangular lattice of $(m + 1) \times (n + 1)$ uniformly spaced control points, \mathbf{P}_{ij} , is placed around an initial aerofoil. Then, given an undeformed domain $\mathcal{A}(x, z) \in [x_{min}, x_{max}] \times [z_{min}, z_{max}]$, the initial control point positions are defined as

$$\mathbf{P}_{ij}^{initial} = \left(x_{min} + \frac{i}{m} (x_{max} - x_{min}), z_{min} + \frac{j}{n} (z_{max} - z_{min}), 0 \right) \quad (2)$$

for $i = 0, \dots, m, j = 0, \dots, n$.

The two-dimensional Bèzier surface, $\Psi(u, v)$, spanning the deformed domain $\mathcal{D}(x, z)$, is then given by

$$\Psi(u, v) = \sum_{j=0}^n \sum_{i=0}^m B_{i,m}(u) B_{j,n}(v) \mathbf{P}_{ij} \quad (3)$$

where $u, v \in [0, 1]$ and $B_{i,m}$ are Bernstein polynomials.

To create the one-to-one deformation mapping required, the undeformed domain \mathcal{A} is then normalised to the unit domain $\mathcal{N}(u, v) \in [0, 1] \times [0, 1]$ by the transformation

$$u(x) = \frac{x - x_{min}}{x_{max} - x_{min}}, \quad v(z) = \frac{z - z_{min}}{z_{max} - z_{min}}, \quad (4)$$

which implies that the required deformation transformation, from $\mathcal{A}(x, z) \rightarrow \mathcal{D}(x, z)$, is given by

$$\Psi(u(x), v(z)) = \sum_{j=0}^n \sum_{i=0}^m B_{i,m}(u(x)) B_{j,n}(v(z)) \mathbf{P}_{ij}. \quad (5)$$

The deformation of the initial aerofoil with respect to the control point positions \mathbf{P}_{ij} is therefore defined as

$$\mathbf{X} = \sum_{j=0}^n \sum_{i=0}^m B_{i,m}(\mathbf{x}^{initial}) B_{j,n}(v(\mathbf{z}^{initial})) \mathbf{P}_{ij} \quad (6)$$

where $(\mathbf{x}^{initial}, \mathbf{z}^{initial})$ represents the initial aerofoil coordinates.

For this paper this method has been implemented with four rows in the control point lattice. This configuration has been used as it was shown to provide the most efficient coverage of the aerofoil design space⁴⁹. Movement of each control point has been restricted to the z -direction and symmetry has been preserved by pairing equivalent upper and lower control points symmetrically to a single design variable. The number of design variables for each case is therefore equal to twice the number of columns in the control point lattice. Figure 2a shows an example deformation for an 8 design variable configuration with associated basis functions shown in 2b.

B. B-Splines

B-Splines are a widely used method for producing piecewise polynomial curves. Much like many of the other parametrisation methods, B-Splines rely on a set of basis functions, however in this case, the coefficients are defined spatially by a set of discrete control points $\mathbf{P}_i \in \mathbb{R}^3$. Given these assumptions a B-Spline curve parametrised by the scalar $u \in [r_0, r_l]$, is defined as

$$X(u) = \sum_{i=0}^{n-1} N_{i,p}(u) \mathbf{P}_i \quad (7)$$

where the $n = l - k$ basis functions of order k are given by

$$N_{i,0}(u) = \begin{cases} 1 & r_i \leq u < r_{i+1} \\ 0 & \text{otherwise} \end{cases}, \quad (8)$$

$$N_{i,k}(u) = \frac{u - r_i}{r_{i+k} - r_i} N_{i,k-1}(u) + \frac{r_{i+k+1} - u}{r_{i+k+1} - r_{i+1}} N_{i+1,k-1}(u), \quad (9)$$

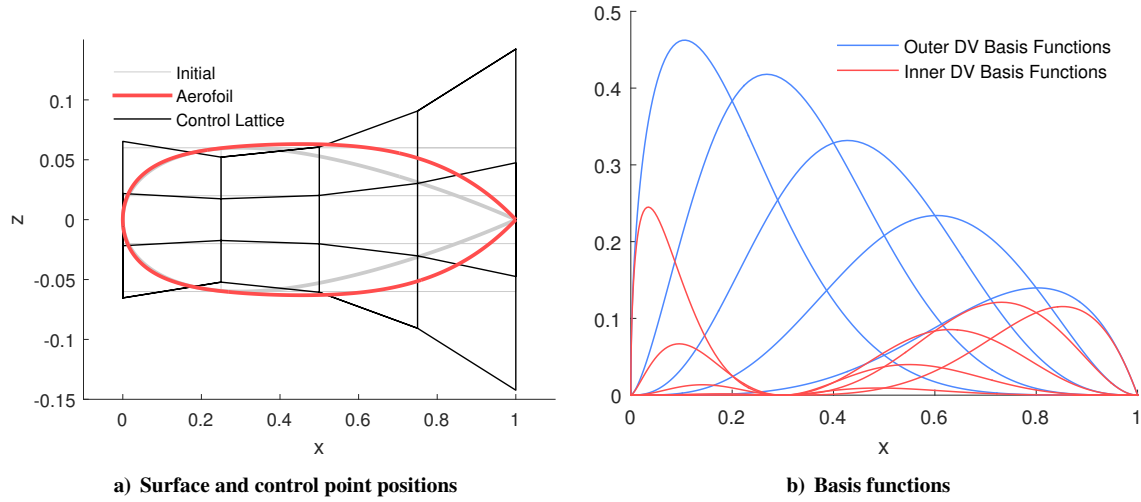


Figure 2. Example deformation of 4×6 Bèzier surface control lattice and NACA0012.

with the increasing knot vector

$$\mathbf{r} = [r_0, \dots, r_l], \quad r_i \leq r_{i+1}. \quad (10)$$

The knot vector then takes the form

$$\mathbf{u} = [\underbrace{r_0, \dots, r_0}_{k+1}, r_{k+1}, \dots, r_{n-1}, \underbrace{r_l, \dots, r_l}_{k+1}] \quad (11)$$

where the values r_{k+1}, \dots, r_{n-1} indicate the knot points where the basis functions meet. In this case, the B-Spline uniformity requires that the knots r_k, \dots, r_n are equally distributed. Additionally if $k = n$, and consequently $l = 0$, the B-Splines are called ‘Bèzier Curves’ and if $u \in [0, 1]$ the basis functions are the Bernstein polynomials of order $k - 1$.

A useful property of B-Splines is that the basis order k controls the locality of the influence of the control points, meaning that for a low order curve the influence of any change in control point position will be more localised compared to if a high order curve was used. Using low order splines can, however, impact the smoothness and overall fidelity of the curve.

B-splines can be used to represent aerofoils in a variety of different ways but for this study each aerofoil is represented by two distinct B-splines. For each B-spline \mathbf{P}_0 is fixed at the leading edge $(0, 0)$, \mathbf{P}_{n+1} is at the trailing edge $(1, 0)$ and \mathbf{P}_1 is aligned vertically with the leading edge. The other points \mathbf{P}_i are then distributed on a half cosine scale between $(0, 1)$ in the chord-wise direction and only allowed to vary in the vertical direction, i.e.

$$\mathbf{P}_0 = (0, 0), \quad \mathbf{P}_i = \left(\frac{1}{2} \left[1 - \cos \left(\frac{\pi(i-1)}{n+1} \right) \right], a_i \right), \quad \mathbf{P}_{n+1} = (1, 0), \quad (12)$$

where a_i denotes a design variable. Again symmetrical control points are paired to create one design variable that controls the local thickness of the aerofoil. Figure 3 shows an example of this configuration.

C. Class Function/ Shape Function Transformations (CST)

The CST method was developed by Kulfan^{5,6} primarily as a method of defining a wide range of aerofoils with relatively few design variables; however, the method can also be extended to other shapes such as square-like and circle-like objects. Each surface is defined as

$$z(x) = C_{N2}^{N1}(x) \cdot S_{upper}(x) + x \cdot z_{te} \quad (13)$$

where the class function

$$C_{N2}^{N1}(x) = x^{N1} \cdot (1 - x)^{N2}, \quad (14)$$

and z_{te} defines the trailing edge half thickness and $x \in [0, 1]$.

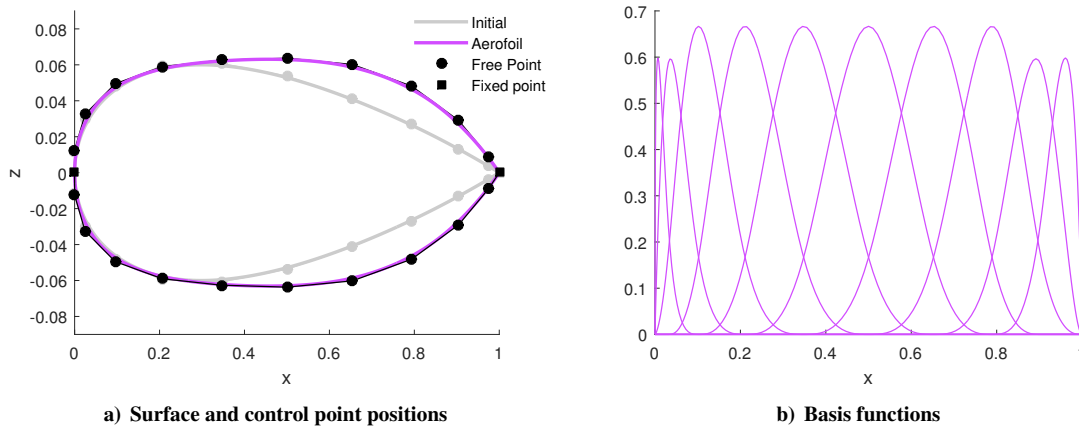


Figure 3. Example deformation of a cubic B-Spline configuration with 10 symmetric design variables.

The values of $N1$ and $N2$ control the overall shape of the parameterisation, where a value of 1 creates a sharp edge, 0.5 a rounded edge and $0 < \epsilon \ll 1$ a flat box shape. The aerofoil class is therefore defined by $N1 = 0.5$ and $N2 = 1$, giving the round leading edge and sharp trailing edge required.

Kulfan⁵⁰ suggested defining $S(x)$ as the linear combination of Bernstein polynomials i.e.

$$S(x) = \sum_{i=0}^n a_i B_{i,n}(x) \quad (15)$$

where

$$B_{i,n}(x) = \binom{n}{i} x^i (1-x)^{n-i}, \quad (16)$$

a_i is the Bernstein coefficient and n is the degree of the polynomials. The class of Bernstein polynomials are a set of single sign C^n continuous functions defined on the interval $x \in [0, 1]$ and, in this region, are mathematically equivalent to the set of standard polynomials of the form $c_i x^i$.

Kulfan⁵¹ later presented a leading edge modification (LEM) to the CST method, including an extra polynomial and coefficient, to improve the fidelity at the leading edge. This proposed adding an additional shape term such that

$$S(x) = \sum_{i=0}^n a_i B_{i,n}(x) + a_{n+1} x^{0.5} (1-x)^{n-0.5}. \quad (17)$$

For the tests performed in this paper the leading edge modification was always used. This is done because, in other work from the authors⁴⁹, it was shown that the leading edge modification significantly helps improve geometric accuracy for aerofoils with high or low leading edge radius. Previous work on this case⁴⁸ suggests that a very large leading edge radius can be expected. The upper and lower surfaces will again be taken to be symmetric, reducing the number of design variables by half. The basis functions for a six design variable CST configuration are shown in 4a.

D. Hicks-Henne Bump Functions

Hicks-Henne bump functions use a base aerofoil definition plus a linear combination of a set of n basis functions defined between 0 and 1 to determine the final aerofoil shape. Each surface is defined by

$$\mathbf{z} = \mathbf{z}^{initial} + \sum_{i=0}^n a_i \phi_i(x) \quad (18)$$

for basis functions $\phi_i(x)$ and coefficients a_i for $i = 1, \dots, n$.

The basis functions proposed by Hicks and Henne⁴ were the sine functions

$$\phi_i(x) = \sin^{t_i} \left(\pi x^{\ln(0.5)/\ln(h_i)} \right), \quad (19)$$

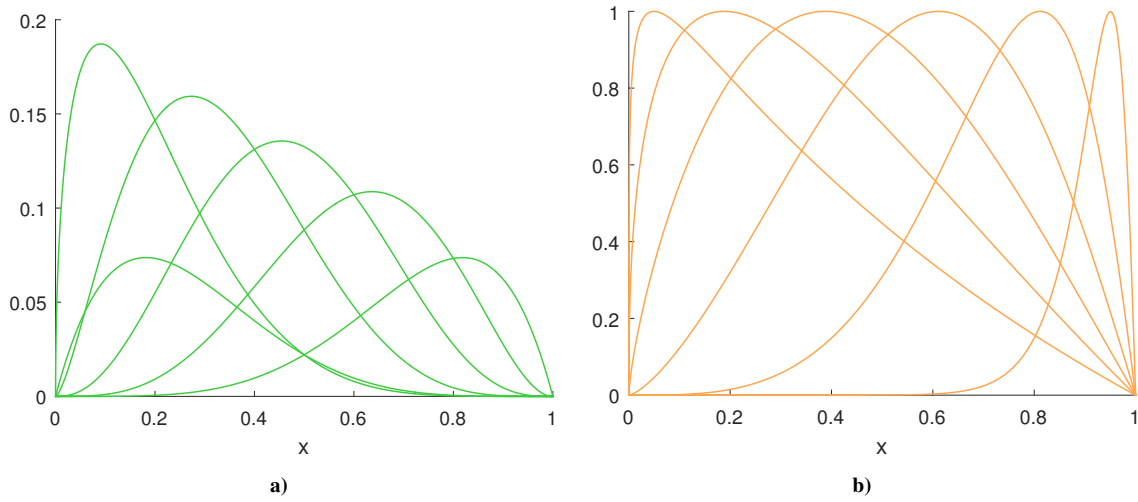


Figure 4. Basis functions for six design variable configurations of the CST method (a) and Hicks-Henne bump functions (b).

where h_i is the location of the maxima of the basis function and t_i controls the width of the functions. Each bump function is therefore defined by three variables, each of which can be optimised or fixed. It is however preferable in many cases to fix both the position and width as this ensures the parameterisation is a linear function of the design variables; this is the approach used here. The bump positions will be defined as

$$h_i = \frac{1}{2} \left[1 - \cos\left(\frac{i\pi}{n+1}\right) \right], \quad i = 1, \dots, n. \quad (20)$$

as used by Wu⁷ and Masters^{49,52} and thickness parameters will be set to $t_i = 1$.

Due to the symmetry of the problem being investigated the upper and lower surface design variables were again taken to be equal.

E. Radial Basis Function Domain Element Method

The RBF domain element (RBF-DE) approach is a full domain deformation method like the Bèzier surface, so creates new aerofoil shapes based on the deformation of an initial aerofoil. The deformation method itself differs however, deforming by preserving the exact movement of a set of control points then creating a deformation field defined by radial basis function interpolation. The general theory of RBFs is outlined by Wendland⁵³ and Buhmann⁵⁴; the formulation used here is presented extensively in Rendall and Allen² and its use as a parametrisation technique in Morris *et al.*³⁴.

The general solution for the deformation is given by

$$\Gamma(X) = \sum_{i=1}^n \beta_{DE_i} \phi(\|X - X_{DE_i}\|) + \mathbf{p}(X) \quad (21)$$

where DE_i indicates the i th domain element control point, X_{DE_i} its centre and β_{DE_i} its coefficient vector. $\mathbf{p}(X)$ is a linear polynomial used to ensure that translation and rotation are captured without added shape deformation.

The coefficients β_{DE_i} are found by requiring the exact recovery of the original function when the control points are in their original positions. The system is then completed by the additional requirement

$$\sum_{i=1}^N \beta_{DE_i} \cdot \mathbf{q}(X) = 0 \quad (22)$$

where $\mathbf{q}(X)$ is a polynomial with order less than or equal to $\mathbf{p}(X)$.

When a discrete set of points in the original domain is to be transformed the problem can be formulated with matrix multiplication. Exact recovery of original points implies that

$$\mathbf{X}_{DE} = \mathbf{D}\mathbf{A} \quad (23)$$

where

$$\mathbf{X}_{DE} = \begin{pmatrix} 0 & 0 \\ 0 & 0 \\ 0 & 0 \\ \vdots & \vdots \\ x_{DE_N} & z_{DE_N} \end{pmatrix}, \quad \mathbf{\Lambda} = \begin{pmatrix} \eta_0^x & \eta_0^z \\ \eta_x^x & \eta_x^z \\ \eta_z^x & \eta_z^z \\ \beta_{DE_1}^x & \beta_{DE_1}^z \\ \vdots & \vdots \\ \beta_{DE_N}^x & \beta_{DE_N}^z \end{pmatrix} \quad (24)$$

and

$$\mathbf{D} = \begin{pmatrix} 0 & 0 & 0 & 1 & 1 & \cdots & 1 \\ 0 & 0 & 0 & x_{DE_1} & x_{DE_2} & \cdots & x_{DE_N} \\ 0 & 0 & 0 & z_{DE_1} & z_{DE_2} & \cdots & z_{DE_N} \\ 1 & x_{DE_1} & z_{DE_1} & \phi_{DE_1DE_1} & \phi_{DE_1DE_2} & \cdots & \phi_{DE_1DE_N} \\ \vdots & \vdots & \vdots & \vdots & \vdots & \ddots & \vdots \\ 1 & x_{DE_N} & z_{DE_N} & \phi_{DE_NDE_1} & \phi_{DE_NDE_2} & \cdots & \phi_{DE_NDE_N} \end{pmatrix} \quad (25)$$

with

$$\phi_{DE_iDE_j} = \begin{cases} \phi(\|X_{DE_i} - X_{DE_j}\|/S_R) & \text{for } \|X_{DE_i} - X_{DE_j}\| \leq S_R \\ 0 & \text{for } \|X_{DE_i} - X_{DE_j}\| > S_R \end{cases} \quad (26)$$

indicating the basis function on the distance between X_{DE_i} and X_{DE_j} and the subscript DE representing a domain element control point. S_R denotes the support radius which specifies the radius of the influence of each control point.

To locate the deformed points the following matrix must be formed where the subscript a indicates the original position of an aerofoil point:

$$\mathbf{A} = \begin{pmatrix} 1 & x_{a_1} & z_{a_1} & \phi_{a_1DE_1} & \phi_{a_1DE_2} & \cdots & \phi_{a_1DE_N} \\ \vdots & \vdots & \vdots & \vdots & \vdots & \ddots & \vdots \\ 1 & x_{a_N} & z_{a_N} & \phi_{a_NDE_1} & \phi_{a_NDE_2} & \cdots & \phi_{a_NDE_N} \end{pmatrix}. \quad (27)$$

The matrix of the deformed aerofoil points, \mathbf{X}^{deform} , is then calculated as

$$\mathbf{X}^{deform} = \mathbf{A}\mathbf{\Lambda} \quad (28)$$

$$= \mathbf{A}\mathbf{D}^{-1}\mathbf{X}_{DE} \quad (29)$$

$$= \mathbf{H}\mathbf{X}_{DE}. \quad (30)$$

Note that as \mathbf{H} is invariant of the current control point positions it only needs to be calculated once. It should be noted that this method can also be applied without the first three ‘polynomial’ rows or columns. The effect of this is that translations and rotations are not retained exactly but it ensures that deformations do not propagate past the support radius.

There are a few factors that affect the use of the RBF-DE method for reconstructing aerofoils; the support radius, the radial basis function, the initial aerofoil used, the number and initial position of the control points as well as the direction of their movement. For this study a support radius of 1 chord will be used throughout as well a radial basis function of Wendland’s C2 function

$$\phi(r) = (1 - r)^4(4r + 1). \quad (31)$$

This leaves the positions of the initial control point positions to be defined. Contrary to the Bèzier surface method where the control points must be defined on a fixed uniform lattice, the initial RBF-DE control points can be placed anywhere. This flexibility gives the user great control over the influence and locality of the deformation though means that a comprehensive search for their best locations is challenging⁵⁵.

For this study, two different initial control point schemes have been considered. A set of ‘off surface’ control points defined on an ellipse around the aerofoil and a set of ‘on surface’ control points defined on the surface of the initial NACA0012, both shown in figure 5. For both configurations it should be noted that each configuration always contains the points included in the coarser levels with an additional set of bisecting points. Similarly to the other methods the design variables are chosen to be the symmetric pairs moving symmetrically in the z direction to create a local thickness change. Additionally for the ‘on surface’ configuration the control points at the leading and trailing edges are held stationary.

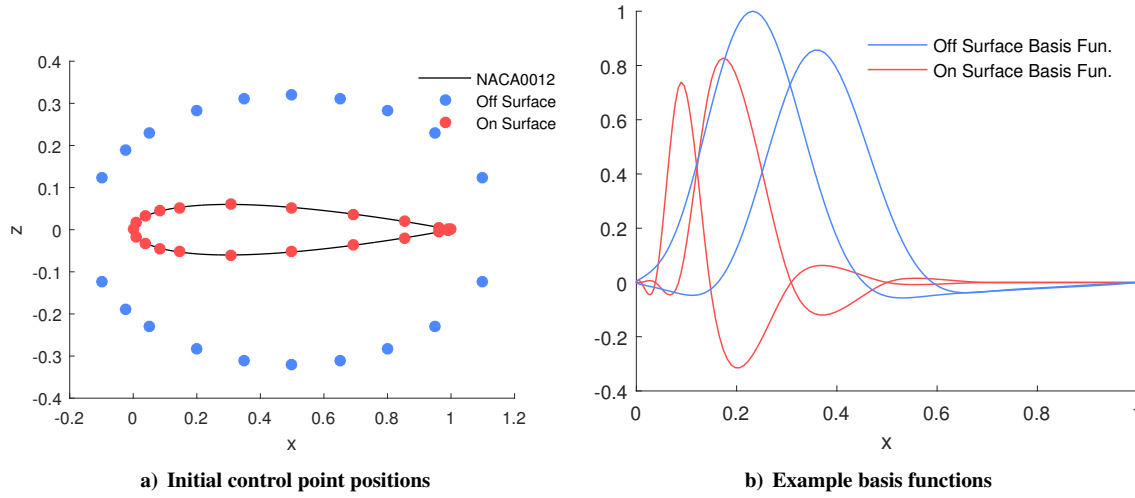


Figure 5. Comparison of ‘on surface’ and ‘off surface’ RBF-DE configurations for 10 symmetric design variables.

F. Singular Value Decomposition (SVD) Method

The SVD method uses proper orthogonal decomposition to derive a set of ordered, orthogonal basis modes from a set of pre-determined training aerofoils. New aerofoil shapes can then be constructed as a linear combination of these modes where the fidelity of the construction is determined by the number of modes used. This technique was first employed by Toal *et al.*³¹ then by Ghoman *et al.*³² and Poole *et al.*³³. Ghoman *et al.*³² used a series of supercritical aerofoils to derive the modes and showed that other supercritical aerofoils could efficiently be reconstructed. Poole *et al.*³³ then extended this to show that a broad range of aerofoils could be represented given a wide choice of training aerofoils.

When constructing the aerofoil shape modes it is crucial that the training library is normalised such that the aerofoil shapes are defined equivalently and discretized by the same number of points. In this work they are transformed to have a sharp trailing edge and discretized such that all the aerofoils have an equal distribution of points along the x -axis. This second condition means that, in this instance, the modes only need to be constructed in the z direction.

To formulate these modes the z coordinates of the training aerofoils are first used to form the rows of the matrix

$$\mathbf{T} = \begin{bmatrix} z_1^1 & z_2^1 & \cdots & z_N^1 \\ z_1^2 & z_2^2 & \cdots & z_N^2 \\ \vdots & \vdots & \ddots & \vdots \\ z_1^M & z_2^M & \cdots & z_N^M \end{bmatrix} \quad (32)$$

for M training aerofoils each of length N .

This matrix is then decomposed into the singular value decomposition

$$\mathbf{T} = \mathbf{U} \cdot \mathbf{\Sigma} \cdot \mathbf{V} \quad (33)$$

where columns of $\mathbf{V} = [\mathbf{v}_1, \mathbf{v}_2, \dots, \mathbf{v}_{\min(N,M)}]$ represent the ordered, orthogonal aerofoil modes and the diagonal values of $\mathbf{\Sigma}$ represent the energy of each mode. The energy is a measure of the importance of the modes within the training library and equivalently can be considered as a ‘typical value’ for its use.

New aerofoils are then constructed as a linear combination of these modes such that

$$\mathbf{z} = \sum_i a_i s_i \mathbf{v}_i \quad (34)$$

for some scaling s_i and where a_i represents the design variables. Two possible scalings are considered in this work, $s_i = 1$ and $s_i = \Sigma_{ii}$.

For this work the training library consisted of all the symmetric aerofoils from the UIUC aerofoil library^b (smoothed and normalised as described in Masters⁵²) and the symmetric NACA 4 series aerofoils with max thickness coefficients from 6 to 24. This made up a training library of 122 aerofoils. The modes produced are shown in figure 6 with the associated energies shown in figure 7.

^bhttp://aerospace.illinois.edu/m-selig/ads/coord_database.html

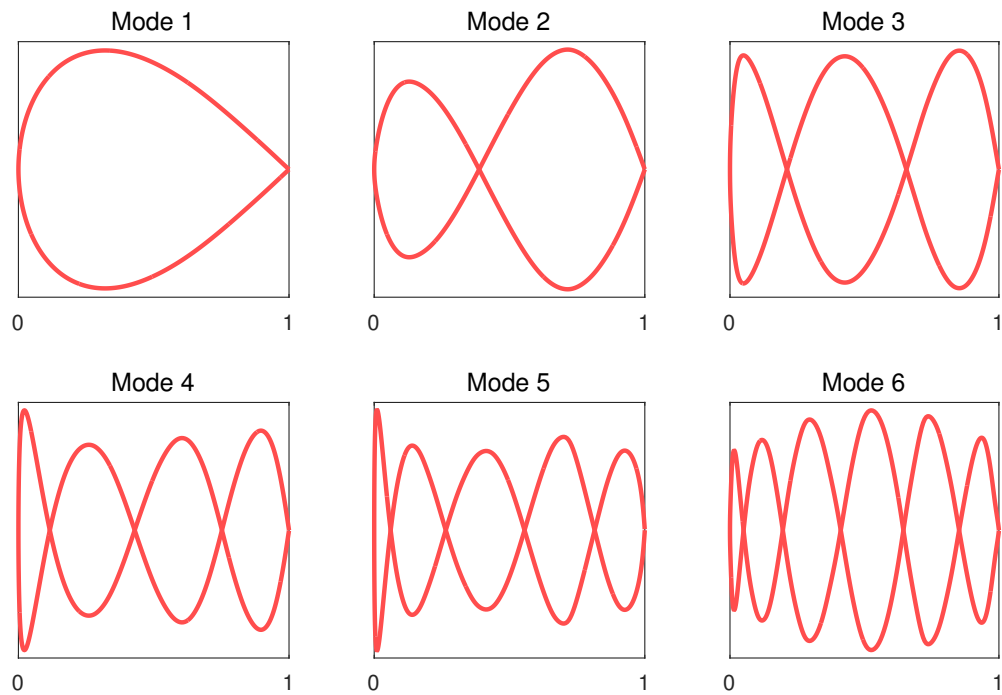


Figure 6. The first 6 SVD modes created with the training library of symmetric aerofoils.

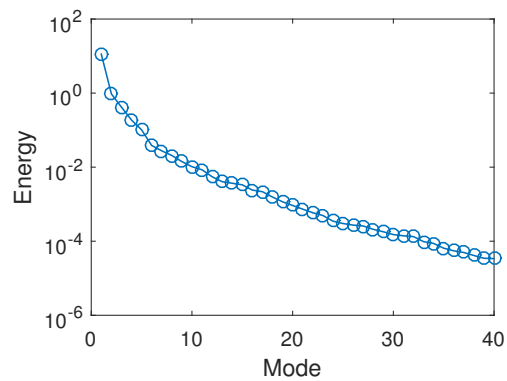


Figure 7. Energy associated with the first 40 SVD modes.

IV. Optimisation Framework

In this work the open-source, unstructured CFD code SU²⁴⁵ was used for all the optimisations, and surface sensitivities were calculated using the continuous adjoint method. Each flow solution was converged down to a maximum change in the drag coefficient of less than 10^{-7} and convergence acceleration was achieved through the use of multigrid. Due to the symmetry of the problem only half of the aerofoil was solved for each simulation with a symmetry condition applied along the line $z = 0$.

The computational meshes were created using a structured O-mesh conformal mapping method with a distance to the far-field of 50 chord lengths and an equal ratio of cells around the aerofoil to cells to the far-field. This creates a final mesh with extremely high orthogonality throughout the volume and a surface cell aspect ratio of one. The original problem specification⁴⁷ recommends that the initial mesh is grid independent to within 0.1 drag counts. A full mesh convergence study for this grid generator is presented in Poole *et al.*⁴⁰, which identified that this condition was sufficiently met for the 257×257 mesh. These tests have been repeated with SU² which confirmed these results. For this reason all of the optimisation procedures were performed with the 257×257 mesh shown in figure 8a. In addition the final results were also run on the finer 513×513 mesh to reduce mesh dependency. These two mesh sizes will be referred to here on after as the ‘optimisation mesh’ and ‘fine mesh’ and are shown in figure 8.

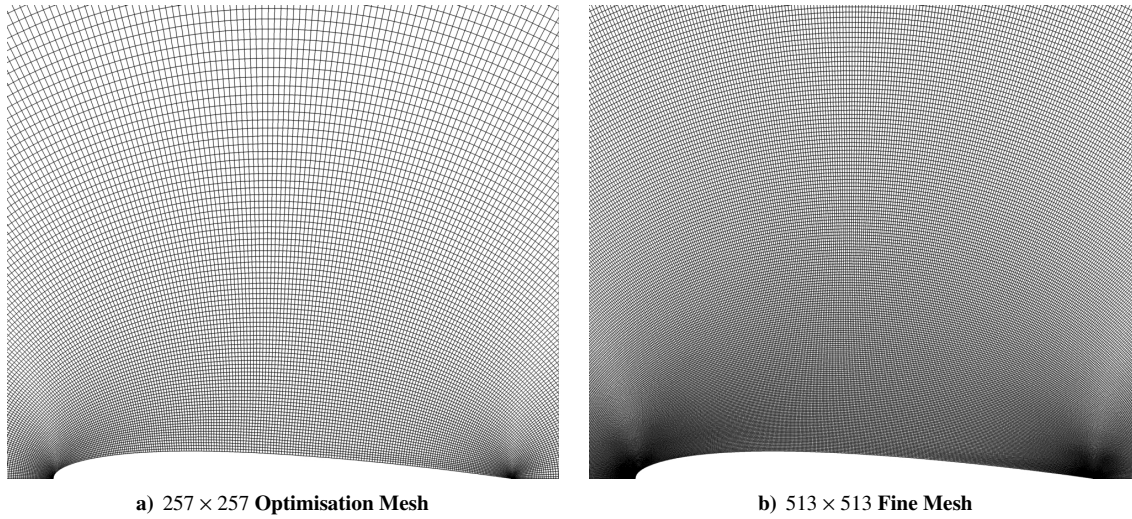


Figure 8. Mesh resolutions used for optimisation (a) and final tests (b).

The optimisation mesh is used for each optimisation procedure throughout with the surface and volume mesh deformed using RBFs⁵⁶ for each flow solve. This is done by applying the same method as for the RBF domain element parameterisation with ‘control points’ placed on each surface point though without the use of the ‘polynomial’ terms. This is applied with a support radius of 10 chord lengths and Wendland’s C4 RBF,

$$\phi(r) = (1 - r)^6(35r^2 + 18r + 1), \quad (35)$$

to ensure the surface deformations are dissipated smoothly across the volume to maintain mesh quality.

The design variable gradients are calculated using the continuous adjoint method⁵⁷ which allows all the gradients to be calculated for a computational cost in the order of one flow solve. This is done by solving the adjoint equations⁴⁵ to calculate the sensitivity of drag coefficient with respect to the unit normal at each surface mesh point, i.e.

$$\frac{\partial C_D}{\partial \mathbf{n}_i} \quad (36)$$

for unit surface normal $\mathbf{n}_i = [n_i^x, n_i^z]$. Then as the surface perturbations in this work will be applied in the z direction only, the surface sensitivities must be projected into the z direction by the transformation

$$\frac{\partial C_D}{\partial z_i} = n_i^z \frac{\partial C_D}{\partial \mathbf{n}_i}. \quad (37)$$

The required gradients of C_D with respect to the design variables, a_i , are then calculated by multiplying this with the

Jacobian of the surface geometry with respect to the chosen design variables,

$$\underbrace{\begin{bmatrix} \frac{\partial C_D}{\partial a_1} \\ \frac{\partial C_D}{\partial a_2} \\ \vdots \\ \frac{\partial C_D}{\partial a_n} \end{bmatrix}}_{\text{Gradients}} = \underbrace{\begin{bmatrix} \frac{\partial z_1}{\partial a_1} & \cdots & \frac{\partial z_m}{\partial a_1} \\ \vdots & \ddots & \vdots \\ \frac{\partial z_1}{\partial a_n} & \cdots & \frac{\partial z_m}{\partial a_n} \end{bmatrix}}_{\text{Geometric Sensitivities}} \underbrace{\begin{bmatrix} \frac{\partial C_D}{\partial z_1} \\ \frac{\partial C_D}{\partial z_2} \\ \vdots \\ \frac{\partial C_D}{\partial z_m} \end{bmatrix}}_{\text{Surface Sensitivities}}. \quad (38)$$

The optimisations were then performed using the multi-purpose large-scale optimiser SNOPT⁴⁶. This is a gradient-based sequential-quadratic programming (SQP) method that employs a reduced-Hessian BFGS search direction and a cubic line-search technique. The surface profile restriction was applied as ‘linear’ constraint and was enforced at every fifth percentile for $x/c \leq 30\%$ and $x/c \geq 40\%$ and every second percentile for $30\% < x/c < 40\%$ as well as at 99% chord. This ensures strict compliance in the maximum thickness region. No explicit bounds are placed on the design variables themselves though their lower limit will be significantly influenced by this thickness constraint.

Convergence of the optimisation was set such that SNOPT terminated from one of two conditions. Either the KKT optimality condition⁴⁶ satisfied the tolerance of 1×10^{-6} or the optimiser was unable to improve the objective function after multiple attempts. It was found for these tests however that this optimality tolerance was never satisfied. For the fewer design variable cases (≤ 8) the optimality was reduced by approximately 2 orders of magnitude and for the higher design variable cases (≥ 12) a reduction of one order was typically achieved. This is consistent with the results achieved by Carrier *et al.*²², Lee *et al.*²⁵ and Telidetzki *et al.*²⁴ for this test case; they also found similar difficulties reducing optimality for other optimisation cases. Therefore in all cases the optimisation was stopped by SNOPT because no further improvement could be made. This is triggered when a total of three consecutive line-search operations yield no improvement. This is sufficient to imply that no further improvement can be made because after two consecutive unsuccessful line-searches the BFGS search direction reduces to the steepest descent method. Thus if no improvement can be made at this point neither the search direction nor the line-search result will change for further iterations and therefore no further improvement can be made.

V. Optimisation Results

A. Initial Optimisation Results

For an initial investigation, design variables sweeps from 4 to 40 were conducted for CST, Bèzier Surface, Cubic B-Spline, Hicks-Henne, RBF-DE on surface and SVD (unit scaled) methods. Figure 9 shows the optimisation results for these cases. It can be seen that there is a clear distinction between the performance of the methods for larger numbers of design variables. The Bèzier surface, CST and Hicks-Henne methods seem to give reasonably consistent results for greater than 20 design variables, whereas the B-Spline, RBF-DE and SVD methods get consistently worse over this period. For all these methods it is clear that better solutions exist than those found by the optimiser; this suggests that the optimiser has been unable to fully exploit the available design space. Figure 10 then shows the optimiser convergence history for the six methods for 36 design variables. At this design point it can be seen that the convergence path for the RBF-DE, B-spline and SVD methods is significantly worse than for the Bèzier surface, CST and Hicks-Henne methods.

To investigate this, the parameterised surface sensitivity was calculated for each method at the optimisation starting point with 40 design variables. This was calculated by multiplying the geometric sensitivities by the design variable gradients. For an unconstrained, steepest descent optimisation this is equivalent to the surface deformation direction, however due to the active profile constraints in this problem this deformation could provide an infeasible shape so merely represents an ‘ideal’ step direction. The parameterised sensitivities for all of the methods have been plotted in figure 11. This figure shows a clear distinction between the Bèzier surface, CST and Hicks Henne methods, and the B-Spline, RBF-DE and SVD methods. The B-Spline, RBF-DE and SVD methods follow the exact adjoint sensitivity much closer than the other methods and as a consequence have significantly sharper, higher frequency curves. For the RBF-DE and B-Spline methods this is because the support of the basis functions reduces as the fidelity increases whereas for the SVD method it is as result of the increasing frequency of the modes. The impact of this is that the resulting surface perturbation may produce surface oscillations and reduce the smoothness of the aerofoil. Importantly the authors use the term ‘smoothness’ in this work in reference to the oscillatory nature of the surface, not its differentiability. It has previously been identified that ensuring the smoothness in the aerofoil optimisation sequence is crucial to the success of aerofoil optimisation^{58,59} and that that unsmooth or oscillatory shapes can lead to non-physical optimisation solutions⁶⁰. This suggests that this capacity to create unsmooth aerofoils may be negatively influencing the optimisation process.

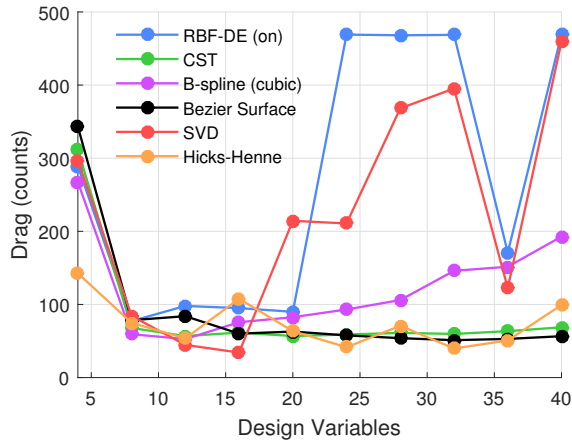


Figure 9. Optimisation results for the initial set of parameterisation configurations.

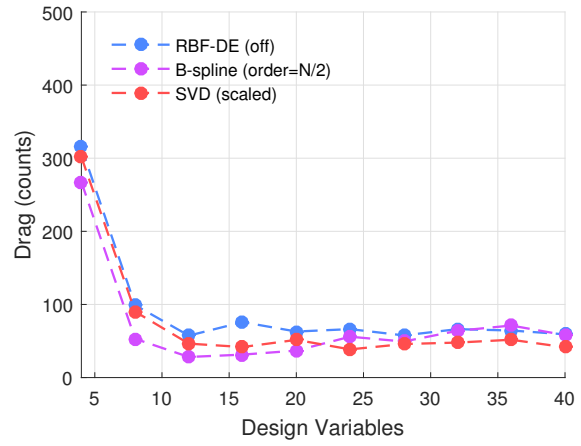


Figure 12. Optimisation results for the improved set of parameterisation configurations.

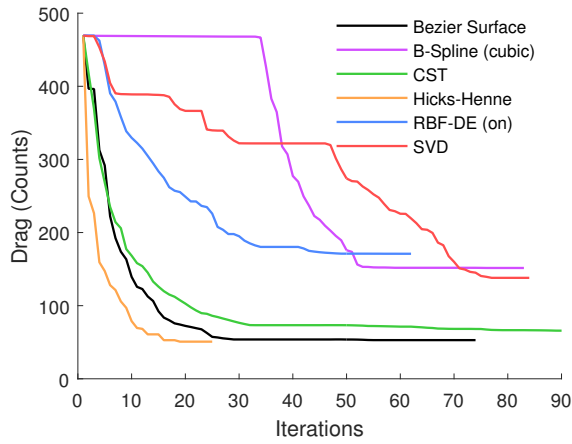


Figure 10. Convergence history for the initial set of parameterisation configurations with 36 design variables.

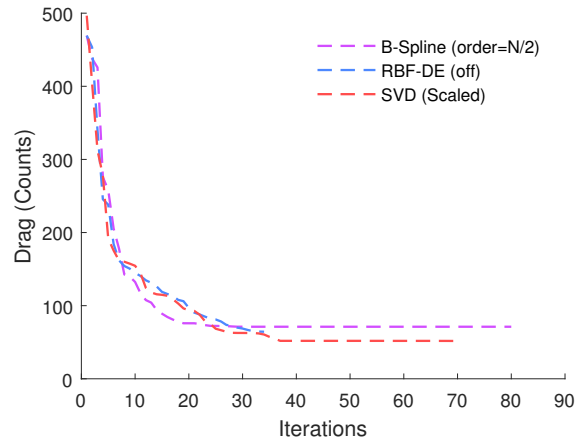


Figure 13. Convergence history for the improved set of parameterisation configurations with 36 design variables.

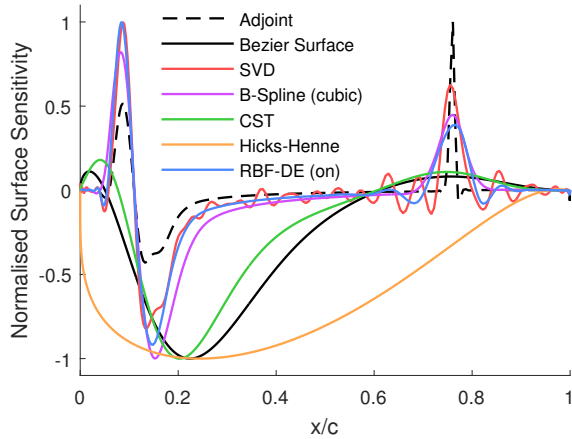


Figure 11. Surface sensitivities on NACA0012 for the initial set of parameterisation configurations for 40 design variables.

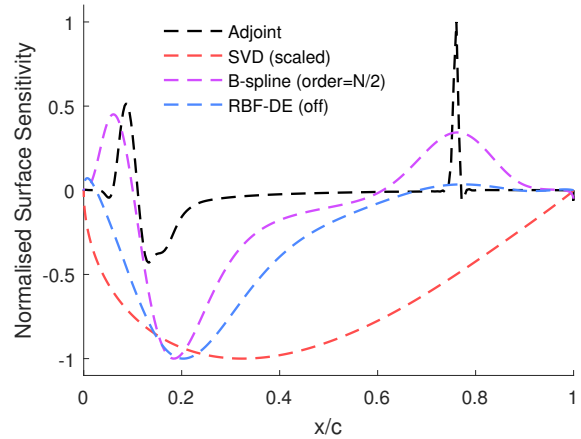


Figure 14. Surface sensitivities on NACA0012 for the improved set of parameterisation configurations for 40 design variables.

To ensure smoother sensitivities were created, two different approaches have been taken. For the RBF-DE and B-spline methods, configurations have been chosen that create larger smoother basis functions. For the RBF-DE method this is done by moving the initial control points positions away from the aerofoil surface and for the B-Spline method a larger polynomial order, equal to half the number of control points, is used. For the SVD method a different approach was taken due to the form of the basis functions; in this case the modes were scaled by the modal energy such that the later, higher frequency modes had a lower maximum value. This benefits the optimisation by ensuring that the design variables are roughly the same order rather than exponentially decreasing.

Figure 14 shows the impact this has on the parameterised surface sensitivities; it can be seen that for the new configurations they are significantly smoother and consequently do not follow the exact adjoint sensitivity as closely. The impact of this on the optimisation results and convergence history at 36 design variables is then shown in figures 12 and 13. Both of these figures show a significant improvement in the results. This suggests that the smoothness of the surface sensitivities has a large impact on the robustness and rate of convergence of this optimisation procedure.

B. Improved Optimisation Results

Figure 15 shows the final optimisation results achieved, with the inclusion of the improved methods for the B-Spline, RBF-DE and SVD methods. These show that the B-Spline method provides the best result with 12 design variables achieving a drag count of 28.2; this equates to a 94% reduction in drag. The other methods, bar Hicks-Henne, seem to produce very similar, consistent, results across the full design variable spectrum investigated, with the SVD method generally attaining a slightly better result than the rest. The Hicks-Henne method on the other hand shows the most variation in results. This may be due to the formation of the basis functions used, as an increase in the number of design variables does not necessarily strictly increase the design space⁴⁹. This can mean that lower design variable solutions are not included in higher design variable space.

Each of the optimum solutions was then re-meshed and run at the fine, 513×513 , mesh resolution to confirm the results and reduce grid dependence. These results can be seen in figure 16. It was expected that all of the results would either decrease or stay the same based on previous work^{23,40}. It can however be seen that for some of the results (indicated by a ▲), a large increase in drag is observed. Figure 17 shows the pressure distributions for two of these cases for the two different mesh resolutions tested. It can be seen that they have produced completely different shock structures near the trailing edge. This may be evidence of non-unique solutions for these aerofoils, similar to the behaviour identified by Meheut *et al.*⁴⁸ and Lee *et al.*²⁵. Further analysis of this is presented in section VII. Ignoring these results it can be seen that figures 15 and 16 show very similar trends with a general reduction in drag shown for the finer mesh. The trends for each of the parameterisation methods are however not what may generally be expected. Drag would be expected to decrease as the number of design variables, and thus the design space, increases. It can however be seen that in many cases this caused the drag to increase. This topic is further investigated in section VI.

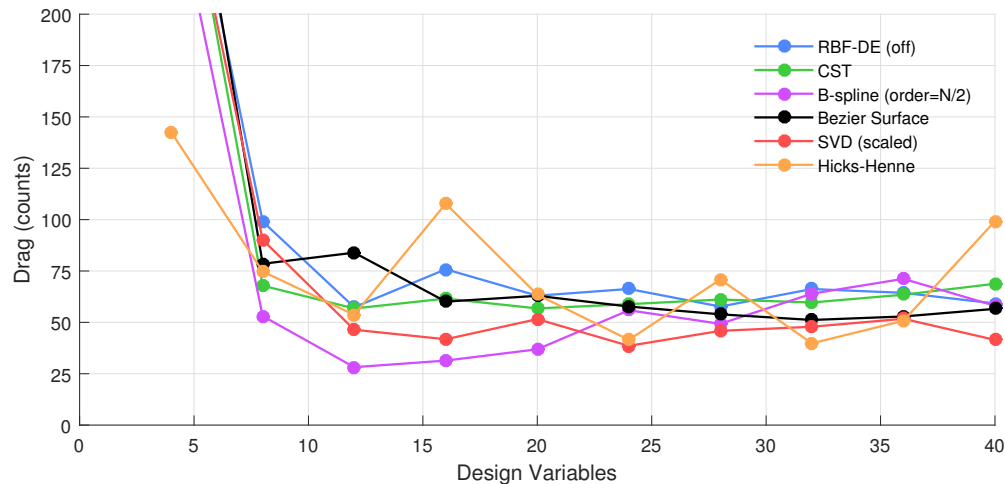


Figure 15. Final optimisation results for each parameterisation method on the 257×257 optimisation mesh.

The best results obtained by each method at the fine mesh resolution are then compared in table 1, from this it can be seen that the B-Spline method gives the best overall result with 16 design variables attaining a drag count of 25.1 counts, which equates to a 95% reduction in drag. The aerofoil shapes and pressure distributions associated

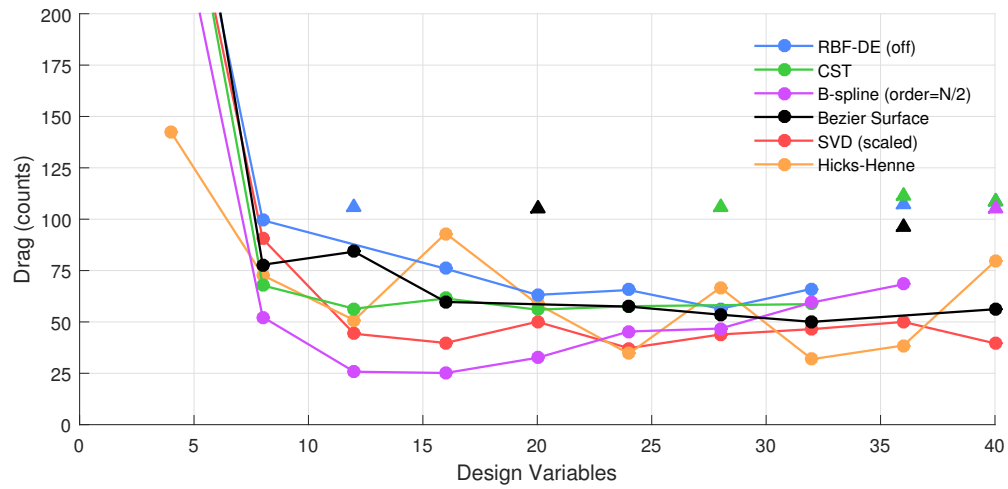


Figure 16. Final optimisation results for each parameterisation method run on the 513×513 fine mesh. \blacktriangle indicates results that have increased in drag due to a change in shock structure.

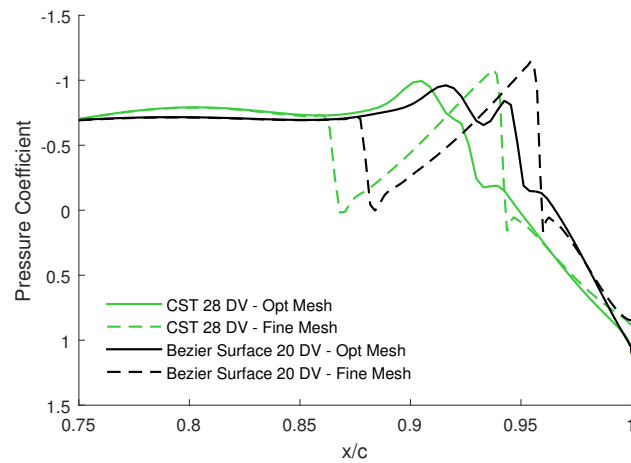


Figure 17. Comparison of trailing edge pressure distributions for two aerofoils at the two mesh resolutions.

with these best results are then shown in figures 18 and 19. From the aerofoil shapes it can be seen that there are two distinct surface results. The two best results, for the B-spline and Hicks-Henne methods, can be seen to have a thicker trailing edge region and an increase in thickness around 50% chord. The other results however maintain the maximum thickness of the original NACA0012 and have slightly thinner shape around the trailing edge; these results produced between 5 and 35 counts more drag. The C_D plots (figure 19) show a similar pattern with the B-Spline and Hicks-Henne giving a different trailing edge shock structure to the other methods. These, lower drag, results display a single normal shock at around 97% chord whereas the other cases appear to form a partially reflected oblique shock at 92% chord followed by a normal shock at 94%. These results are in agreement with the original problem set by Vassberg *et al.*²⁸, where it was believed that this is the lowest Mach number at which a shock free optimized solution is not possible.

Method	# of DVs	C_D (counts) (257x257 mesh)	C_D (counts) (513x513 mesh)
NACA0012	-	469.3	469.4
CST	20	56.8	56.0
Bèzier Surface	32	51.2	50.0
B-Spline (Order = N/2)	16	31.4	25.1
Hicks-Henne	32	39.8	31.9
RBF-DE (off)	28	57.7	56.4
SVD (scaled)	24	38.6	37.2

Table 1. Table showing the best results attained by each method on the 257×257 optimisation mesh and 513×513 refined mesh.

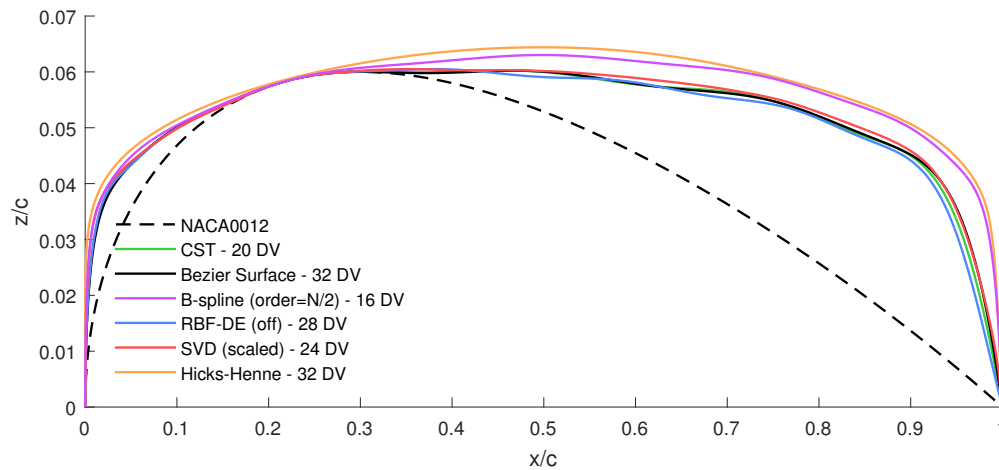


Figure 18. Comparison of the aerofoil shapes for the optimum result achieved with each method.

C. Numerical Drag Approximation

The difference in the results for the two different computational meshes highlights the influence of the mesh on this study. When analysing these effects it is important to consider that the drag calculated will be made up of two components; the physical drag and the numerical drag. The physical drag is the component calculated as a result of the flow effects, in this case the wave drag associated with the shocks, whereas the numerical drag is the component created purely through numerical error. As the numerical drag should not be influenced significantly by the Mach number and a shock-free solution will give exactly zero wave drag, the numerical drag can be approximated by reducing the Mach number to below its critical value. Figure 20 shows a sweep of Mach number for the best aerofoil geometry with the 257×257 optimisation mesh and 513×513 fine mesh. For both cases it can be seen that the drag converges to a constant value for low Mach numbers; this should just be the numerical drag remaining. For the optimisation mesh this indicates a numerical drag of around 20 drag counts whereas for the fine mesh it indicates just 0.2 counts. It is important to reiterate here that the two different meshes used represent a difference in topology as well as resolution. The optimisation mesh is created around the initial NACA0012 and is then deformed in the z direction so that the

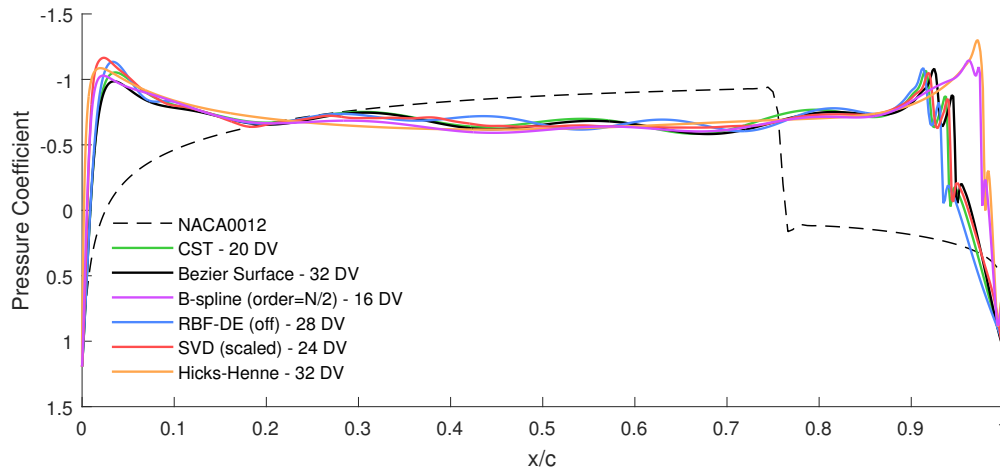


Figure 19. Comparison of the aerofoil shapes for the optimum result achieved with each method

surface matches the desired geometry, this can result in a reduction in mesh quality. The fine mesh however is created directly from the optimised geometry thus represents a significantly higher quality mesh. It is likely that both the increased resolution and mesh quality are factors in the reduction of numerical drag. In particular this highlights the improvement in accuracy achieved by re-meshing the final optimised aerofoil geometries.

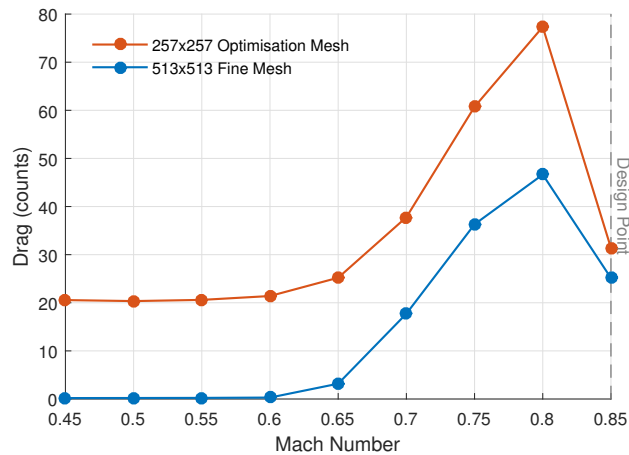


Figure 20. Drag calculated for 'optimum' solution (B-Spline 16 DVs) for a range of Mach numbers.

VI. Geometric Approximation of Best Aerofoil

The optimisation results presented in figures 15 and 16 show the unexpected behaviour that the optimised drag results do not monotonically decrease for an increase in design variables. In fact for the B-Spline method, which produced the best result, the results monotonically increase for 16 or more design variables. There are two explanations for this, either the optimisation does not always achieve the global minimum or the increased design space does not always contain an equal or better solution.

To investigate this a geometric study has been performed that uses a linear least squares approximation to approximate the 'optimum' aerofoil produced (B-spline 16 DV) with all of the parameterisation methods used. This gives an indication of how close the design spaces are to the optimum design found. It is not however guaranteed to give feasible or smooth aerofoils. The difference between the aerofoils is computed as the root-mean-squared distance between the surface points and is presented in figure 21, it should be noted that the 16 design variable B-spline case is omitted as it is the 'optimum' aerofoil and thus there is no error. The filled markers represent feasible aerofoils (to a maximum total error tolerance of 10^{-4}) while the unfilled markers represent infeasible aerofoils. Furthermore a CFD simulation has been run for each of these approximate aerofoils to calculate the drag associated with them. This was

done using the 513×513 fine mesh and the procedure used for the re-meshed optimisation results. These results are shown in figure 22.

The geometric results in figure 21 show that all of the methods reduce the geometric error for every four parameter increase in the design variables. This indicates that in the vicinity of the best solution the design space is increasing for all of the parameterisation methods as would be expected. It can however be seen that this happens at different, but consistent, rates for each method. The CFD results in figure 22 then show that for all of the approximations within an RMS error of 10^{-4} produce results very close to the ‘optimum’ aerofoil. Crucially this shows that these aerofoils are within the design space of the parametrisations so could have been found by the optimisations.

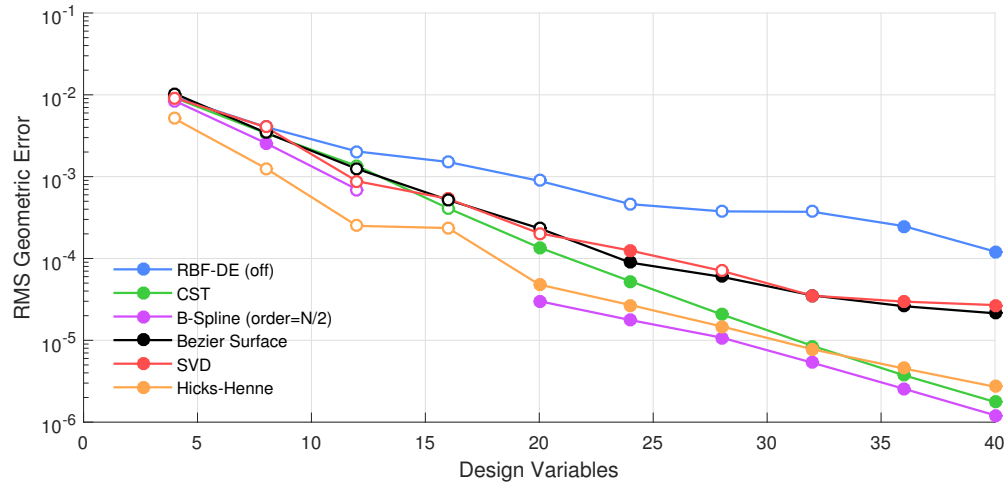


Figure 21. Comparison of the RMS geometric error between the best solution attained and the least squares approximation for each parametrisation.

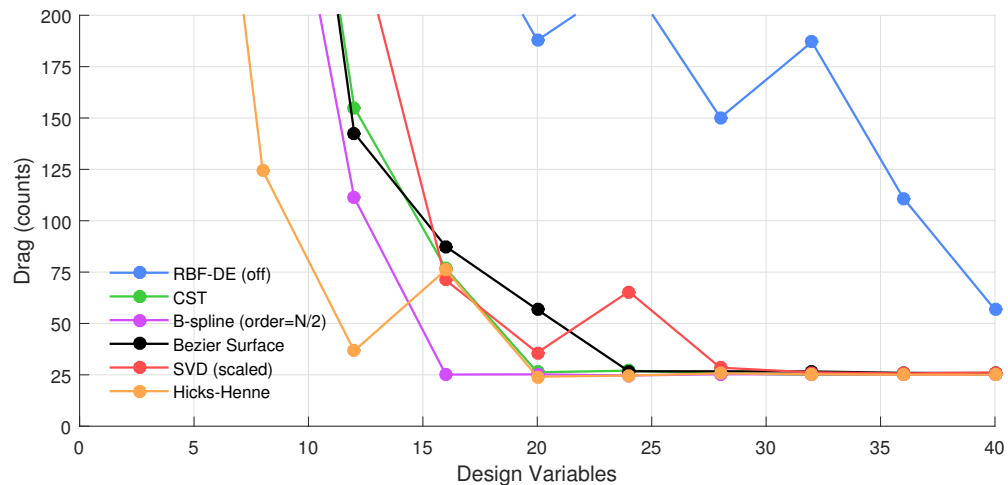


Figure 22. Drag calculated for least squares approximations of best solution.

VII. Mesh Convergence and Hysteresis Study

It can be seen from figure 18 that the six different parameterisation methods tested produce two distinct optimised shapes. The CST, Bèzier Surface, RBF-DE and SVD methods produce a shape with a lower thickness over the aft half of the aerofoil chord with a shallower boat-tail angle, whilst the B-spline, Hicks-Henne and SVD methods produce a thicker aerofoil with a higher boat-tail angle. The thicker of the two distinct shapes produced drag values of around 25-30 counts on the fine mesh. The other, slightly thinner shape, produces drag values between 35 and 55 counts on the fine mesh.

To validate the results a mesh convergence study was performed on an example of each of the two distinct designs. The best results for the B-spline method (order=N/2, 16 DV) and Bèzier surface method (32 DV) were the two aerofoils

tested. The fine 513×513 mesh was used as a base for this study and was coarsened twice in each direction to produce three distinct mesh levels: 513×513 , 257×257 and 129×129 . The results of the mesh convergence studies are shown in table 2, corresponding results for the initial NACA0012 are also shown.

Mesh Density	C_D (counts)		
	NACA0012	B-spline	Bèzier Surface
129×129	487.5	38.5	60.8
257×257	471.7	27.8	51.2
513×513	469.4	25.1	50.0

Table 2. Table of mesh convergence results.

As discussed in section II.B Meheut *et al.*⁴⁸ and Lee *et al.*²⁵ identified hysteresis in some of the highly optimised shapes for the problem discussed in this work. In both cases this was found by sweeping up in Mach number from a point below the 0.85 design point to a point above it then sweeping back down in the previous direction, each time starting the CFD simulation from the previous solution. It was found that around the original design point two solutions existed with different drag counts (~ 50 and ~ 120). Jameson⁶¹ and Kuzmin *et al.*⁶² illustrate that hysteresis of this nature occurs when a small perturbation in flow conditions motivates the splitting or amalgamation of a supersonic zone, creating a discontinuous transition between structures. They further show that this transition point can be dependant on the direction of the changing flow condition, thus resulting in non-unique solutions. Further research on this topic is investigated in^{63–65}.

To investigate hysteresis in the two aerofoil sections highlighted (those designed using B-spline and Bèzier surface parameterisations) a sweep in Mach number up and down between 0.849 and 0.851 is performed. The sweep is performed on both the 129×129 mesh and the 257×257 mesh, and the results are shown in figure 23. It is interesting to note that the hysteresis occurs at a very small window of freestream Mach number and is highly mesh dependent. For example, for the B-spline parameterised aerofoil on the 257×257 mesh, there is no hysteresis at the design point, and instead this occurs at a lower Mach number. The Mach flow contours are shown in figures 24 for both aerofoils on the 129×129 mesh (both the upper and lower branches are shown on the same plot). The upper branch of both of the aerofoils has a double shock flow structure with drag values approximately double the lower branch, which has a single shock. This is in agreement with findings of Jameson⁶¹ and Kuzmin *et al.*⁶² who suggested that this behaviour is caused by the transition between single and double supersonic zones. The difference in shock strength and structure between these aerofoils and the initial flow shown in figure 1 also highlights the significant changes made as a result of the optimisation.

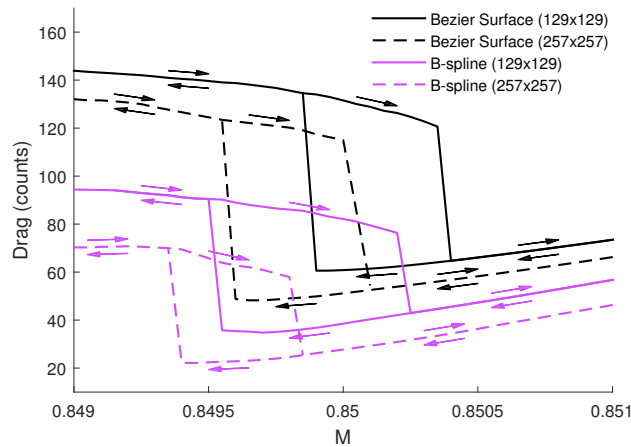
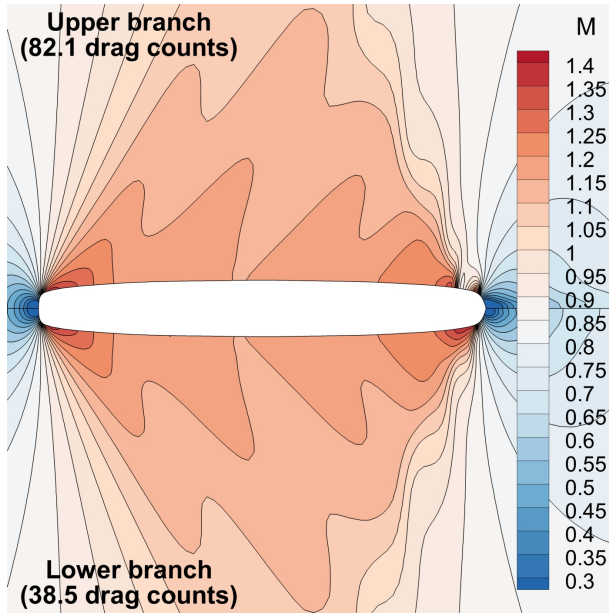


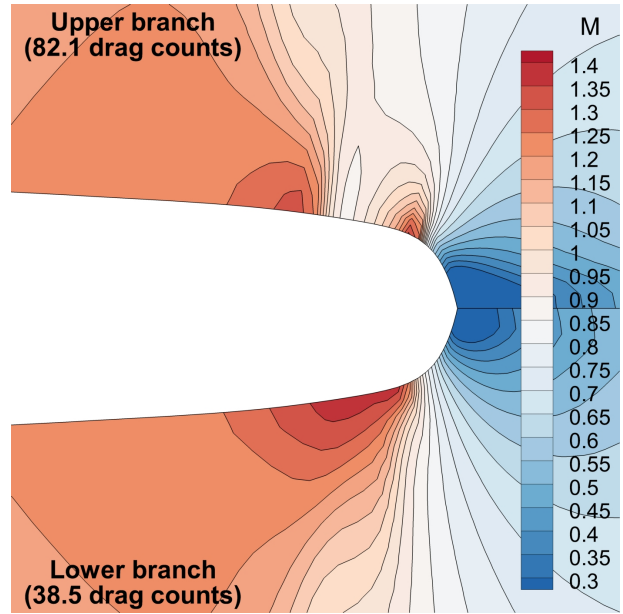
Figure 23. Hysteresis loops produced for small Mach sweeps.

VIII. Conclusions

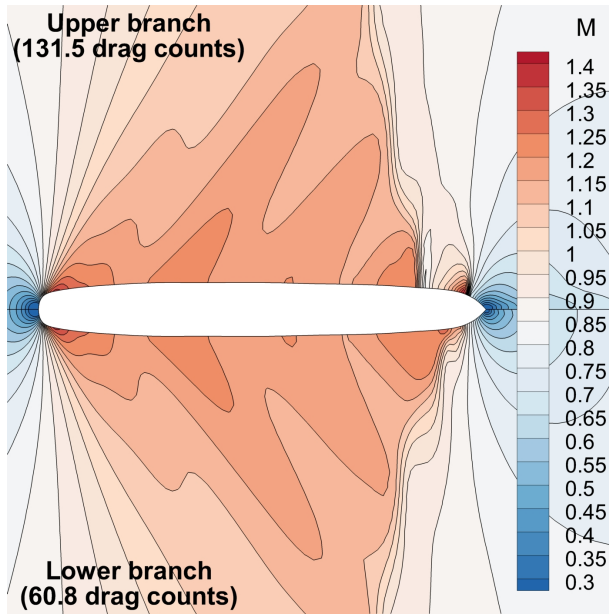
In this work the AIAA Aerodynamic Design Optimisation Discussion Group NACA0012 symmetric, inviscid drag optimisation benchmark case has been run with six different parameterisation methods (B-splines, Bèzier surfaces, CST, Hicks-Henne, RBF-DE and SVD) with between 4 and 40 design variables. Firstly it was found that the smoothness had a significant impact on the robustness and rate of convergence of the optimisations, with the capacity for some of



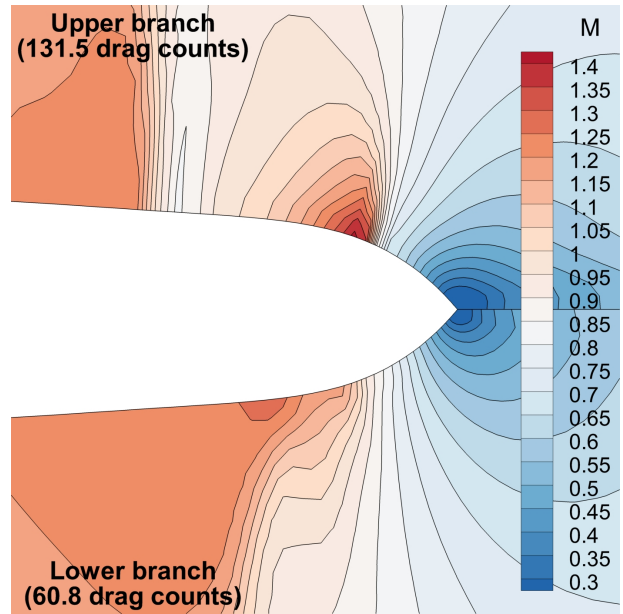
a) B-spline



b) B-spline Trailing Edge



c) Bèzier Surface



d) Bèzier Surface Trailing Edge

Figure 24. Flowfield plots at $M = 0.85$ at upper and lower flow branches on 129×129 mesh.

the parameterisation methods to create unsmooth aerofoils negatively impacting their results for higher design variables. This led to improvements for the B-spline and RBF-DE methods, by increasing the support of the basis functions and, for the SVD method, by reducing the influence of the higher frequency modes.

A set of final optimisation results were then presented at two mesh resolutions; a 257×257 mesh used for the optimisations themselves and a fine 513×513 mesh. They showed that the best result was achieved by the B-spline method with 16 design variables, producing a result with 25.1 drag counts on the 513×513 mesh. Two distinct surface solutions were found with the B-spline and Hicks-Henne methods producing a thicker, larger boat-tail angle compared to those produced by the Bèzier surface, CST, RBF-DE and SVD methods. The thicker shapes correlate with lower drag results and different shock structures.

A geometric study was performed on the best aerofoil shape found where it was approximated with each of parameterisation methods for the design variable range used for optimisation. Drag results were then calculated for all of these approximations. This showed that for all of the methods better results could be obtained than were found in the optimisations and for all methods, apart from the RBF-DE method, drag-equivalent results to the optimum aerofoil were achieved with more than 28 design variables.

A further investigation of the hysteretic behaviour encountered was then presented for the best results achieved with the B-spline and Bèzier surface methods. This showed that for both aerofoils hysteresis loops could be formed by sweeping up and down in Mach number within a range of ± 0.001 of the $M = 0.85$ design point.

IX. Acknowledgements

This work was carried out using the computational facilities of the Advanced Computing Research Centre, University of Bristol - <http://www.bris.ac.uk/acrc/>. The authors also wish to acknowledge the financial support provided by Innovate UK: the work reported herein has been undertaken in GHandI (TSB 101372), a UK Centre for Aerodynamics project.

References

- [1] Sóbester, A. and Forrester, A. I., *Aircraft Aerodynamic Design: Geometry and Optimization*, John Wiley & Sons, 2014.
- [2] Rendall, T. C. S. and Allen, C. B., “Unified fluid–structure interpolation and mesh motion using radial basis functions,” *International Journal for Numerical Methods in Engineering*, Vol. 74, No. 10, 2008, pp. 1519–1559, doi: 10.1002/nme.2219.
- [3] Jameson, A., “Aerodynamic design via control theory,” *Journal of Scientific Computing, also ICASE Report No.88-64*, Vol. 3, 1988, pp. 233–260, doi: 10.1007/BF01061285.
- [4] Hicks, R. M. and Henne, P. A., “Wing design by numerical optimization,” *Journal of Aircraft*, Vol. 15, No. 7, 1978, pp. 407–412, doi: 10.2514/3.58379.
- [5] Kulfan, B. M., “Universal parametric geometry representation method,” *Journal of Aircraft*, Vol. 45, No. 1, 2008, pp. 142–158, doi: 10.2514/1.29958.
- [6] Kulfan, B. M. and Bussioletti, J. E., “Fundamental parametric geometry representations for aircraft component shapes,” *11th AIAA/ISSMO Multidisciplinary Analysis and Optimization Conference*, September 2006.
- [7] Wu, H.-Y., Yang, S., Liu, F., and Tsai, H.-M., “Comparison of three geometric representations of airfoils for aerodynamic optimization,” *16th AIAA Computational Fluid Dynamics Conference, Orlando, Florida*, 2003.
- [8] Kim, S., Alonso, J., and Jameson, A., “Two-dimensional high-lift aerodynamic optimization using the continuous adjoint method,” *Multidisciplinary Analysis Optimization Conferences*, American Institute of Aeronautics and Astronautics, Sept. 2000.
- [9] Bogue, D. and Crist, N., “CST Transonic Optimization using Tranair++,” 2008.
- [10] Lane, K. and Marshall, D., “A Surface Parameterization Method for Airfoil Optimization and High Lift 2D Geometries Utilizing the CST Methodology,” *Aerospace Sciences Meetings*, American Institute of Aeronautics and Astronautics, Jan. 2009.
- [11] Ceze, M., Hayashi, M., and Volpe, E., “A study of the CST parameterization characteristics,” 2009.
- [12] Lane, K. A. and Marshall, D. D., “Inverse Airfoil Design Utilizing CST Parameterization,” *48th AIAA Aerospace Sciences Meeting*, 2010.
- [13] Hewitt, P. and Marques, S., “Aerofoil Optimisation Using CST Parameterisation in SU2,” *Royal Aeronautical Society Biennial Applied Aerodynamics Research Conference, 2014*, 2014.

- [14] Leifsson, L. T., Koziel, S., Tesfahunegn, Y. A., Hosder, S., and Gramanzini, J.-R., "Application of Physics-Based Surrogate Models to Benchmark Aerodynamic Shape Optimization Problems," *53rd AIAA Aerospace Sciences Meeting*, Jan 2015.
- [15] Fabiano, E. and Mavriplis, D. J., "Adjoint-Based Aerodynamic Design On Unstructured Meshes," *54th AIAA Aerospace Sciences Meeting*, Jan 2016.
- [16] Fusi, F., Quaranta, G., Guardone, A., and Congedo, P. M., "Drag minimization of an isolated airfoil in transonic inviscid flow by means of genetic algorithms," *53rd AIAA Aerospace Sciences Meeting*, Jan 2015.
- [17] Zhang, Y., Han, Z.-H., Shi, L., and Song, W.-P., "Multi-round Surrogate-based Optimization for Benchmark Aerodynamic Design Problems," *54th AIAA Aerospace Sciences Meeting*, Jan 2016.
- [18] Song, W. and Keane, A. J., "A study of shape parameterisation methods for airfoil optimisation," *10th AIAA/ISSMO Multidisciplinary Analysis and Optimization Conference*, 2004, pp. 2031–2038.
- [19] Sherar, P., Thompson, C., Xu, B., and Zhong, B., "An Optimization Method Based On B-spline Shape Functions & the Knot Insertion Algorithm." *World congress on engineering*, Citeseer, 2007, pp. 862–866.
- [20] Lépine, J., Trépanier, J.-Y., and Pépin, F., "Wing aerodynamic design using an optimized NURBS geometrical representation," *The 38th AIAA Aerospace Sciences Meeting and Exhibit*, No. AIAA–2000–699, Reno, Nevada, 2000.
- [21] Bisson, F. and Nadarajah, S., "Adjoint-Based Aerodynamic Optimization of Benchmark Problems," *52nd Aerospace Sciences Meeting*, Jan 2014.
- [22] Carrier, G., Destarac, D., Dumont, A., Meheut, M., Salah El Din, I., Peter, J., Ben Khelil, S., Brezillon, J., and Pestana, M., "Gradient-based aerodynamic optimization with the elsA software," *52nd Aerospace Sciences Meeting*, Jan 2014, doi: 10.2514/6.2014-0568.
- [23] Nadarajah, S., "Adjoint-Based Aerodynamic Optimization of Benchmark Problems," *53rd AIAA Aerospace Sciences Meeting*, Jan 2015.
- [24] Telidetzki, K., Osusky, L., and Zingg, D. W., "Application of Jetstream to a Suite of Aerodynamic Shape Optimization Problems," *52nd Aerospace Sciences Meeting*, Jan 2014.
- [25] Lee, C., Koo, D., Telidetzki, K., Buckley, H., Gagnon, H., and Zingg, D. W., "Aerodynamic Shape Optimization of Benchmark Problems Using Jetstream," *53rd AIAA Aerospace Sciences Meeting*, 2015.
- [26] Gariépy, M., Trepanier, J.-Y., Malouin, B., and Tribes, C., "Direct Search Airfoil Optimization Using Far-Field Drag Decomposition Results," *53rd AIAA Aerospace Sciences Meeting*, Jan 2015.
- [27] Zhang, M., Rizzi, A. W., and Nangia, R. K., "Transonic Airfoils and Wings Design Using Inverse and Direct Methods," *53rd AIAA Aerospace Sciences Meeting*, Jan 2015.
- [28] Vassberg, J., Harrison, N., Roman, D., and Jameson, A., "A Systematic Study on the Impact of Dimensionality for a Two-Dimensional Aerodynamic Optimization Model Problem," *29th AIAA Applied Aerodynamics Conference*, Jun 2011.
- [29] Ren, J., Thelen, A. S., Amrit, A., Du, X., Leifsson, L. T., Tesfahunegn, Y., and Koziel, S., "Application of Multifidelity Optimization Techniques to Benchmark Aerodynamic Design Problems," *54th AIAA Aerospace Sciences Meeting*, Jan 2016.
- [30] Sobieczky, H., "Parametric airfoils and wings," *Recent Development of Aerodynamic Design Methodologies*, Springer, 1999, pp. 71–87.
- [31] Toal, D. J. J., Bressloff, N. W., Keane, A. J., and Holden, C. M. E., "Geometric filtration using proper orthogonal decomposition for aerodynamic design optimization," *AIAA Journal*, Vol. 48, 2010, pp. 916–928, doi: 10.2514/1.41420.
- [32] Ghoman, S. S., Wan, Z., Chen, P. C., and Kapania, R. K., "A POD-based reduced order design scheme for shape optimization of air vehicles," *53rd AIAA/ASME/ASCE/AHS/ASC Structures, Structural Dynamics and Materials Conference*, 2012.
- [33] Poole, D. J., Allen, C. B., and Rendall, T. C. S., "Metric-based mathematical derivation of efficient airfoil design variables," *AIAA Journal*, Vol. 53, No. 5, 2015, pp. 1349–1361, doi: 10.2514/1.J053427.
- [34] Morris, A. M., Allen, C. B., and Rendall, T. C. S., "CFD-based optimization of aerofoils using radial basis functions for domain element parameterization and mesh deformation," *International Journal for Numerical Methods in Fluids*, Vol. 58, No. 8, Nov 2008, pp. 827–860, doi: 10.1002/flid.1769.
- [35] Morris, A., Allen, C., and S. Rendall, T., "Domain-Element Method for Aerodynamic Shape Optimization Applied to Modern Transport Wing," *AIAA journal*, Vol. 47, No. 7, 2009, pp. 1647–1659.

- [36] Allen, C. B. and Rendall, T. C. S., “CFD-based optimization of hovering rotors using radial basis functions for shape parameterization and mesh deformation,” *Optimization and Engineering*, Vol. 14, No. 1, Mar 2013, pp. 97–118, doi: 10.1007/s11081-011-9179-6.
- [37] Chauhan, D., Praveen, C., and Duvigneau, R., “Wing shape optimization using FFD and twist parameterization,” *12th Aerospace Society of India CFD Symposium*, 2010.
- [38] Amoignon, O., Hradil, J., and Navratil, J., “Study of parameterizations in the project CEDESA,” *52nd Aerospace Sciences Meeting*, Jan 2014.
- [39] Anderson, G. R., Nemec, M., and Aftosmis, M. J., “Aerodynamic Shape Optimization Benchmarks with Error Control and Automatic Parameterization,” *53rd AIAA Aerospace Sciences Meeting*, Jan 2015.
- [40] Poole, D. J., Allen, C. B., and Rendall, T. C. S., “Control Point-Based Aerodynamic Shape Optimization Applied to AIAA ADODG Test Cases,” *53rd AIAA Aerospace Sciences Meeting*, Jan 2015.
- [41] Leifsson, L. T., Koziel, S., and Hosder, S., “Aerodynamic Design Optimization: Physics-based Surrogate Approaches for Airfoil and Wing Design,” *52nd Aerospace Sciences Meeting*, Jan 2014.
- [42] Poole, D. J., Allen, C. B., and Rendall, T. C. S., “Application of control point-based aerodynamic shape optimization to two-dimensional drag minimization,” *52nd Aerospace Sciences Meeting*, 2014, doi: 10.2514/6.2014-0413.
- [43] LeDoux, S. T., Vassberg, J. C., Young, D. P., Fugal, S., Kamenetskiy, D., Huffman, W. P., Melvin, R. G., and Smith, M. F., “Study Based on the AIAA Aerodynamic Design Optimization Discussion Group Test Cases,” *AIAA Journal*, Feb 2015, pp. 1–26.
- [44] Rendall, T. C. S. and Allen, C. B., “Efficient mesh motion using radial basis functions with data reduction algorithms,” *Journal of Computational Physics*, Vol. 228, No. 17, 2009, pp. 6231–6249.
- [45] Palacios, F., Alonso, J., Duraisamy, K., Colonno, M., Hicken, J., Aranake, A., Campos, A., Copeland, S., Economon, T., Lonkar, A., Lukaczyk, T., and Taylor, T., “Stanford University Unstructured (SU²): An open-source integrated computational environment for multi-physics simulation and design,” *Aerospace Sciences Meetings*, American Institute of Aeronautics and Astronautics, Jan. 2013.
- [46] Gill, P. E., Murray, W., and Saunders, M. A., “SNOPT: An SQP algorithm for large-scale constrained optimization,” *SIAM journal on optimization*, Vol. 12, No. 4, 2002, pp. 979–1006.
- [47] Nadarajah, S., “Aerodynamic Design Optimization: Drag Minimization of the NACA 0012 in Transonic Inviscid Flow,” Retrieved from <https://info.aiaa.org/tac/ASG/APATC/AeroDesignOpt-DG/Test%20Cases/ADODG%20Case%201%20and%202%20NACA0012%20and%20RAE%202822.pdf>.
- [48] Meheut, M., Destarac, D., Carrier, G., Anderson, G., Nadarajah, S., Poole, D., Vassberg, J., and Zingg, D. W., “Gradient-Based Single and Multi-points Aerodynamic Optimizations with the elsA Software,” *53rd AIAA Aerospace Sciences Meeting*, Jan 2015.
- [49] Masters, D. A., Taylor, N. J., Rendall, T. C. S., Allen, C. B., and Poole, D. J., “A Geometric Comparison of Aerofoil Shape Parameterisation Methods,” *54rd AIAA Aerospace Sciences Meeting*, Jan 2016.
- [50] Kulfan, B. M., “A universal parametric geometry representation method-CST,” *45th AIAA Aerospace Sciences Meeting and Exhibit*, January 2007.
- [51] Kulfan, B. M., “Modification of CST airfoil representation methodology,” Retrieved from <http://www.brendakulfan.com/docs/CST8.pdf>.
- [52] Masters, D. A., Taylor, N. J., Rendall, T. C. S., Allen, C. B., and Poole, D. J., “Review of Aerofoil Parameterisation Methods for Aerodynamic Shape Optimisation,” *53rd AIAA Aerospace Sciences Meeting*, Jan 2015, doi: 10.2514/6.2015-0761.
- [53] Wendland, H., *Scattered data approximation*, Cambridge University Press Cambridge, 2005.
- [54] Buhmann, M. D., “Radial basis functions,” *Acta numerica*, Vol. 9, 2000.
- [55] Poole, D. J., Allen, C. B., and Rendall, T. C. S., “Optimal Domain Element Shapes for Free-Form Aerodynamic Shape Control,” *53rd AIAA Aerospace Sciences Meeting*, 2015, doi: 10.2514/6.2015-0762.
- [56] Rendall, T. C. S. and Allen, C. B., “Parallel efficient mesh motion using radial basis functions with application to multi-bladed rotors,” *International journal for numerical methods in engineering*, Vol. 81, No. 1, 2010, pp. 89–105.

- [57] Jameson, A., “Advances in aerodynamic shape optimization,” *Computational Fluid Dynamics 2004*, Springer, 2006, pp. 687–698.
- [58] Jameson, A., “Aerodynamic shape optimization using the adjoint method,” *Lectures at the Von Karman Institute, Brussels*, 2003.
- [59] Schmidt, S., Ilic, C., Gauger, N., and Schulz, V., “Shape gradients and their smoothness for practical aerodynamic design optimization,” *Optim. Eng.(20 08) Preprint-Number SPP1253-10-03*, 2008.
- [60] Mohammadi, B. and Pironneau, O., “Shape optimization in fluid mechanics,” *Annu. Rev. Fluid Mech.*, Vol. 36, 2004, pp. 255–279.
- [61] Jameson, A., “Airfoils Admitting Non-unique Solutions to the Euler Equations,” *AIAA 22nd Fluid Dynamics, Plasmadynamics and Lasers Conference*, Honolulu, Hawaii, 1991, AIAA Paper 91–1625.
- [62] Kuzmin, A. G. and Ivanova, A. V., “The structural instability of transonic flow associated with amalgamation/splitting of supersonic regions,” *Theoretical and Computational Fluid Dynamics*, Vol. 18, No. 5, 2004, pp. 335–344.
- [63] Jameson, A., Vassberg, J. C., and Ou, K., “Further Studies of Airfoils Supporting Non-Unique Solutions in Transonic Flow,” *AIAA Journal*, Vol. 50, No. 12, 2012, pp. 2865–2881.
- [64] Ou, K., Jameson, A., and Vassberg, J. C., “Airfoils Supporting Non-unique Transonic Solutions for Unsteady Viscous Flows,” *7th AIAA Theoretical Fluid Mechanics Conference*, Atlanta, Georgia, 2014, AIAA Paper 2014–2927.
- [65] Kuzmin, A., “Bifurcations of transonic flow past flattened airfoils,” 2009.